

pubs.acs.org/JPCC Article

Sensitivity Analysis of Electrochemical Double Layer Approximations on Electrokinetic Predictions: Case Study for CO Reduction on Copper

Published as part of The Journal of Physical Chemistry C virtual special issue "Jens K. Nørskov Festschrift". Andrew Jark-Wah Wong, Bolton Tran, Naveen Agrawal, Bryan R. Goldsmith, and Michael J. Janik*



Cite This: J. Phys. Chem. C 2024, 128, 10837-10847



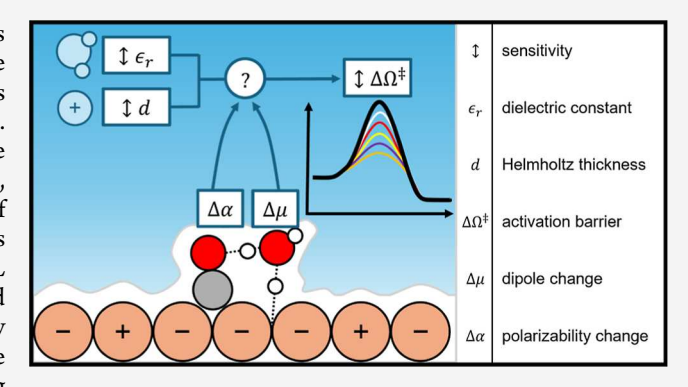
ACCESS I

III Metrics & More

Article Recommendations

Supporting Information

ABSTRACT: Density functional theory (DFT) modeling has been useful to electrocatalyst research, yet simulating the complexities of the electrode-electrolyte interface hinders progress in understanding reaction mechanisms and the underlying kinetics. Though many approaches to incorporating electrochemical double layer (EDL) features in DFT calculations have been developed, uncertainty in interfacial solvent properties and the distribution of ions leave the impact of the EDL on electrocatalytic kinetics unclear. Elucidating the sensitivity of DFT predictions to the EDL properties and model is crucial. Herein, we use an analytical Grand Canonical DFT framework (aGC-DFT) to quantify the sensitivity of potential-dependent activation energies to parameters of the EDL, incorporating a Helmholtz EDL model with varying



dielectric constant (ε_r) and EDL width (d). We compute the activation barriers for OC-H, CO-H, and OC-CO bond formation from CO* on Cu. These elementary reactions are critical within the heavily debated reaction mechanism of CO2 reduction and are likely to impact overall activity and product selectivity. We show the aGC-DFT method produces consistent results with explicit GC-DFT calculations, while enabling probing of the EDL model sensitivity at a much lower computational cost. Reaction steps with significant dipole moment changes (i.e., CO-H bond formation) are highly sensitive to the chosen EDL parameters, such that the relative barriers of the OC-H, CO-H, and OC-CO bond formation steps depend significantly on EDL properties. Without knowledge of the interfacial properties of the EDL, there is substantial uncertainty in activation barriers and elementary reaction rates within a DFT analysis of electrocatalytic kinetics.

1. INTRODUCTION

Density functional theory (DFT) modeling has been very useful in determining electrocatalytic reaction mechanisms and guiding the design of electrocatalytic materials. 1-6 However, major challenges exist in modeling the complex potentialdependent interplay between solvent, ions, and adsorbates at the electrode-electrolyte interface, which hinders progress in making accurate predictions of electrokinetics. 7-10 Changes in the composition and structure of the electrode-electrolyte interface, the electrochemical double layer (EDL), impact electrocatalytic activity and selectivity. ^{11–22} Despite advances in modeling the electrocatalytic interface, uncertainties in the solvent properties and ion distributions within the EDL pose challenges in modeling EDL effects. Representing the EDL within a DFT model inherently requires approximations because DFT cannot sample the dynamic ensemble of atomistic structures at the interface. 7,8 Thus, different mechanistic predictions can be reached depending on the DFT and EDL model approximations chosen. This challenge

in modeling electrocatalytic reactions has impacted mechanistic understanding of the carbon dioxide reduction reaction (CO₂RR) on copper, where the mechanism is still heavily debated despite numerous atomistic modeling studies (Figure $1).^{23}$

Different DFT approaches have led to different conclusions about the dominant reaction pathways for the CO₂RR on Cu. Focusing on the reaction mechanism to C₁ products, Nørskov and co-workers (red in Figure 1) predicted from their thermodynamic analysis (within the computational hydrogen electrode framework) that adsorbed CO* preferentially reduces to CHO* and that the (O)C-H bond formation

Received: March 5, 2024 Revised: May 14, 2024 Accepted: June 4, 2024 Published: June 25, 2024





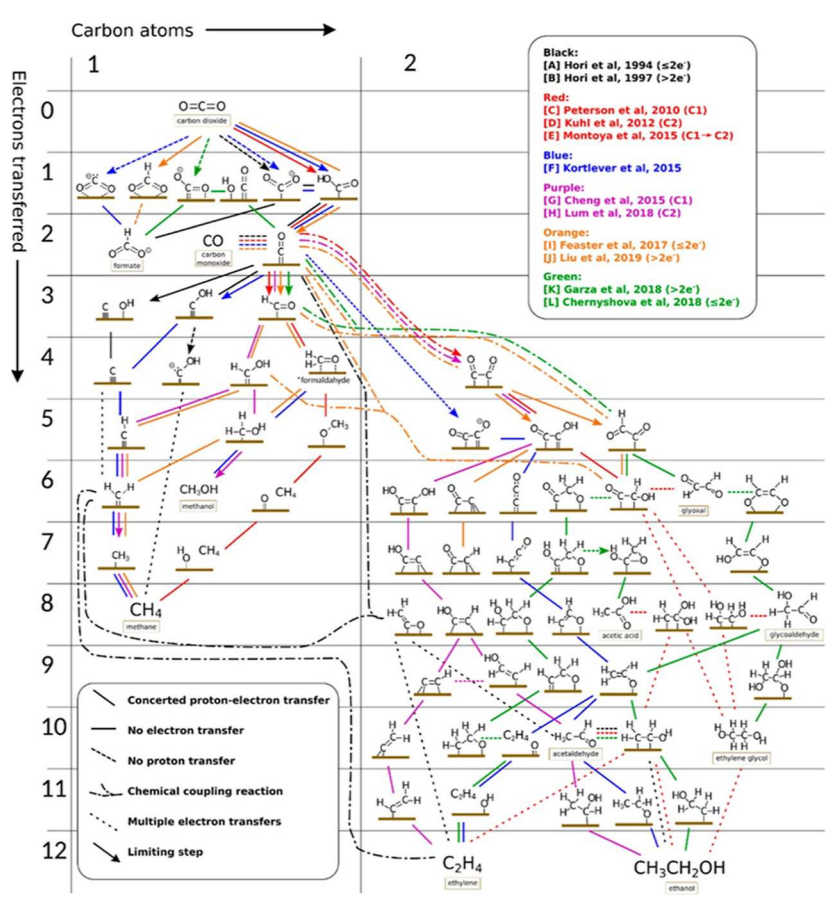


Figure 1. Reaction network of CO_2 electrochemical reduction to C_1 and C_2 products on Cu postulated from different experimental and theoretical studies. Each colored line is a different concluded mechanism from its respective author as shown in the top right legend. Citations of the reaction schemes in the top right legend are denoted here. ^{24–35} Figure 1 is reproduced from ref 23. Copyright American Chemical Society.

pathway is more favorable than (C)O-H bond formation.²⁶ They also concluded that the path through the CHO* adsorbate led to methane formation. However, Schouten et al.³⁶ demonstrated via an electrochemical mass spectrometer experiment that CH2O*, present along this C-H pathway, primarily produces methanol. Nie et al. (blue in Figure 1) calculated electrochemical activation barriers on Cu(111) with one or two explicit H2O to facilitate proton shuttling. In contrast, their study predicted that the O-H pathway is more favorable and leads to methane formation, whereas the C-H pathway leads to methanol.^{37–39} Cheng et al. (purple in Figure 1) proposed an alternate branching mechanism of methane formation from the C-H pathway using ab initio molecular dynamics with metadynamics, explicit water, and implicit solvation.³⁰ Clearly, the chosen model used to approximate the elementary electrokinetics toward C1 leads to qualitatively different conclusions on the overall reaction mechanism. Nevertheless, all studies conclude that the path CO* takes dictates the product selectivity, whether through C-H formation, O-H formation, or OC-CO dimerization to C2 products.

DFT studies with a continuum approximation of the EDL are computationally tractable for electrocatalysis modeling because the complex electrolyte dynamics are represented as a classically averaged, structureless medium. The continuum electrolyte interacts with the charged electrode and adsorbates through mean-field electrostatics and nonelectrostatic approximations. However, such continuum models require para-

metrization, such as the solvent dielectric properties and cavity definition, which are often fitted to reproduce the experimental solvation free energies of organic molecules in bulk solutions. Varying the potential in such models can be accomplished by changing the surface charge, which then necessitates approximations for the distribution of countercharge within the EDL.

In a continuum EDL model, the electrolyte parameters influence the electrochemical interfacial properties and, consequently, the reaction energetics. Nørskov and co-workers highlighted this point by examining various parameters of a polarizable continuum model, such as the dielectric constant and the electron density cutoff for the cavity-shape function. They showed that these parameters affect solvent and ion distributions, the potential of zero charge (PZC), and the EDL capacitance. They found that no single set of parameters using a linearized Poisson-Boltzmann/polarizable continuum model can accurately capture all the underlying physics at the electrochemical interface. For example, correcting for the ion distribution (to not be unphysically close to the electrode) and the interfacial water dielectric constant (to be much lower than the bulk water value) yielded an interfacial capacitance much lower than experimental values. In addition, they reported that the thermodynamics of CO₂ adsorption and the Volmer reaction on Pt(111) depend strongly on the choice of EDL parameters. Zhang and Asthagiri also showed that DFTpredicted overpotentials for the oxygen reduction reaction depend on the parameters used within the VASPSol

continuum solvation model.⁴¹ These examples demonstrate a well-known challenge for predicting electrocatalytic reaction energetics with continuum EDL models: the sensitivity of reaction energetics to the EDL model parameters.^{7–9,41–43}

Despite the above challenge being known to the modeling community, many electrokinetic studies implement only one parameter set in the continuum EDL model without considering the associated sensitivities in the resulting reaction energetics. Gas-phase adsorption energy predictions of monoand diatomic adsorbates using standard generalized gradient approximation functionals generally deviate 0.1–0.2 eV from the experiment. The deviations compared to experiments when modeling electrocatalytic processes are surely larger when considering the challenges in representing the impact of solvation, electrification, and their potential-dependent intricacies. Consequently, the uncertainty in reaction energetics associated with EDL model sensitivity exacerbates conflicting predictions of CO₂RR pathways (Figure 1).

Quantifying the sensitivity of reaction energetics may require repeating resource-intensive calculations (e.g., geometry optimizations and transition state searches) with different EDL parameters. This challenging scalability is especially true when multiple calculations for different electrode potentials are performed by using, for example, DFT calculations with a "computational potentiostat". To promote transparency and accessibility, we propose a scalable, accurate, and interpretable way to determine potential-dependent reaction energetic sensitivity to EDL parameters.

In this article, we examine the impact of EDL dielectric properties and ionic charge distribution on the elementary energetics of CO* reduction steps. We use an analytical GC DFT framework (aGC-DFT) to calculate potential-dependent barriers for C-H, O-H, and OC-CO formation of CO* on Cu(111) and Cu(100) surfaces while quantifying the sensitivity based on parameters used to represent the EDL. A simple Helmholtz model is used, with two parameters defining the EDL, the Helmholtz width, and the dielectric constant. We analyze the C-H, O-H, and OC-CO formation involving CO* because the selectivity toward C₁ and C₂ products likely depends on these reactions. We compare these aGC-DFT results to explicit GC-DFT (eGC-DFT) calculations where the GC framework is embedded within the DFT code. Reaction energetics are consistent between the aGC-DFT and eGC-DFT approaches across all three reactions. We discuss the advantages and disadvantages of both approaches for modeling electrocatalysis. aGC-DFT calculations show that activation barriers for reactions with significant surface-normal dipole moment changes are much more sensitive to the choice of the EDL parameters compared to reactions with minimal dipole moment changes. Overall, without knowledge of the interfacial properties of the electrode-electrolyte interface, there is large uncertainty in modeling electrokinetics and electrocatalysis due to the sensitivity of DFT predictions on these parameters. We last discuss opportunities (electrolyte tuning and probing double layer structures) for computational studies in electrocatalysis.

2. METHODS

2.1. Electronic Structure Calculation and Model Construction. *2.1.1. Joint-Density Functional Theory.* For DFT calculations in joint-DFT (JDFTx), the revised Perdew–Burke–Ernzerhof (RPBE) functional was used with the GRBV ultrasoft pseudopotential. ^{50,53,54} A plane-wave energy cutoff of

544 eV was used. A Monkhorst–Pack k-point grid of $4 \times 4 \times 1$ was used to sample the Brillouin zone. S5,56 Electronic convergence was sped up using a Fermi–Dirac smearing with a 0.2 eV width and a convergence threshold of 3×10^{-6} eV energy difference. The ionic optimization converged to 3×10^{-5} eV energy difference or 0.01 eV/Å in root-mean-squared force.

The CANDLE solvation model was used, which is based on a linear polarizable continuum formalism with a nonvarying bulk dielectric constant and a linearized Poisson—Boltzmann ionic distribution. State At the simplest level, this solvation model requires choosing a bulk dielectric constant and ion concentration (assumed ± 1 ionic pair). The default values for each were used, that is, a dielectric constant of 78 and an ion concentration of 1 M, which gives a Debye screening length of 3 Å.

The climbing-image nudged elastic band method (CI-NEB) was used to find transition states. ⁵⁹ CI-NEB was implemented in the atomic simulation environment (ASE), with JDFTx being used as the energy and force calculator. ⁶⁰ CI-NEB calculations converged with a force threshold of 0.05 eV/Å. Vibration calculations were subsequently performed to confirm a single imaginary mode for the transition state.

The following elementary steps of CO reduction were constructed on Cu(111) and Cu(100)

$$CO^* + H^* \rightarrow CHO^*$$
 $(C - H \text{ step})$
 $CO^* + H^* \rightarrow COH^*$ $(O - H \text{ step})$
 $CO^* + CO^* \rightarrow ^*OCCO + ^*$ $(OC - CO \text{ step})$

The Cu(111) and Cu(100) surfaces were modeled as four-layered 3×3 unit cells, where the bottom two layers were frozen at their optimal lattice constants during ionic optimizations. CO* was placed on hollow sites. For the O–H step, one explicit H_2O was used to shuttle the adsorbed H* to the oxygen on CO*. The visualization of the optimized initial, final, and transition states for each reaction step on each surface is in Supporting Information, Note 1.

2.1.2. Vienna Ab Initio Simulation Package. The Vienna Ab Initio Simulation Package (VASP) interface from ASE was used for single-point calculations and transition state searches from JDFTx optimized structures. The single-point calculations were to obtain parameters for the aGC-DFT formalism (see Section 2.2.2). In principle, one does not need to switch electronic structure calculators to obtain the parameters for aGC-DFT. This JDFTx-to-VASP workflow was logistically convenient for our current collaborative work and helps to demonstrate the consistency of results across the two codes. Geometry optimizations performed in VASP were observed to be nearly identical to the JDFTx optimized geometries, as shown in Supporting Information, Note 2.

In VASP, electronic structure calculation settings are kept identical to those in JDFTx, with a few exceptions. The same RPBE functional, plane-wave cutoff of 544 eV, k-point grid of 4 \times 4 \times 1, and electronic convergence threshold of 3 \times 10⁻⁶ eV were used. One main difference is that the projector augmented wave (PAW) method is being used in place of the GRBV pseudopotential. Finally, VASP single-point calculations were performed in a vacuum (i.e., without implicit solvation), necessitating a dipole correction (IDIPOL = 3 and LDIPOL = .TRUE.) in the normal direction to prevent unphysical interactions between periodic images. These

numerical differences between JDFTx for eGC-DFT and VASP for our aGC-DFT calculations do not have a notable effect on comparable reaction energies, as demonstrated by the agreement between the two approaches (as shown in the Results and Discussion). Solvation free energies of intermediates in bulk water were also computed in the VASPSol implicit solvation model using the default parameters (dielectric constant of 78 and Debye length of 3 Å).^{67,68} A comparison between solvation free energies between VASPSol and JDFTx is discussed in Supporting Information, Note 3, showing minimal differences between the two solvation models. Transition state searches were performed using CI-NEB to compare between structures from VASP and JDFTx. The force convergence criteria for all geometry optimizations were set to 0.01 eV Å⁻¹. A single imaginary harmonic mode was verified to confirm transition state structures.

2.2. Potential-Dependent Activation Barriers. 2.2.1. Explicit GC-DFT. Geometry optimizations and CI-NEB searches were performed in JDFT'x at the following applied potentials vs the standard hydrogen electrode (SHE): 0.0, -0.4, -0.8, -1.2, -1.6, and -2.0 V. The applied potential was fixed by setting a target electronic Fermi energy ($\mu_{\rm F}$), which was converted to the SHE scale by using $U_{\rm SHE} = \frac{-\mu_{\rm F} - \phi_{\rm ref}}{1e}$, where $\phi_{\rm ref} = 4.66$ eV, as calibrated to the CANDLE implicit solvation model. ⁵⁸

The potential-dependent (grand free energy) activation barriers are computed using

$$\Delta\Omega^{\ddagger} = \Delta G^{\ddagger} - \mu_{\rm F} \Delta N_{\rm e} \tag{1}$$

 Ω and G denote the grand free energy and Gibbs free energy of a system, respectively. $N_{\rm e}$ and $\mu_{\rm F}$ are the excess number of electrons (varying) and the Fermi energy (preset), respectively. The Δ and the \ddagger superscript indicate the difference between the transition state and the initial state (i.e., the forward activation barrier).

The initial states for the C–H and O–H reaction steps were chosen as $1/2H_2(gas)$ and adsorbed CO*. This essentially describes these reactions as proton-coupled-electron-transfer steps. Finally, at some applied potentials, the final and transition states of certain steps could not be optimized.

2.2.2. Analytical GC-DFT (aGC-DFT). An aGC framework was used to calculate the energetics of species λ corrected to constant potential and with the interactions between the electric field and the adsorbate, as given in eq 2. This methodology was explained in detail in prior work, with the main points reviewed here⁵²

$$\Omega_{\lambda}(U) = G_{\lambda}(U_{\text{pzc},\lambda}) - \frac{1}{2}C_{\text{dl}}(U - U_{\text{pzc},\lambda})^2 + \mu_{\lambda}F_{\lambda} + \frac{1}{2}\alpha_{\lambda}F^2$$
(2)

Here, $G_{\lambda}(U_{\text{pzc},\lambda})$ is the Gibbs free energy of an adsorbed intermediate at the metal/vacuum interface at the PZC of the surface with adsorbate present $(U_{\text{pzc},\lambda})$, with λ in the subscript). The free energies of each species are obtained by eq 3

$$G_{\lambda}(U_{\text{pzc},\lambda}) = E_{\text{DFT}} + E_{\text{ZPVE}} - TS_{\text{vib}}$$
 (3)

where $E_{\rm DFT}$ is the DFT-calculated electronic energy of the species, $E_{\rm ZPVE}$ is the zero-point energy correction, and $TS_{\rm vib}$ is the harmonic vibrational entropic corrections at 300 K (omitting modes with imaginary and less than 50 cm⁻¹ frequency). $C_{\rm dl}$ is the capacitance of the electrochemical double layer, discussed below, and U is the electrode potential. The dipole-field interaction is described by the surface-normal

dipole moment (μ_{λ}) and the electric field (F_{λ}) . The last term is the induced dipole-field interaction described by the polarizability (α_{λ}) and the electric field. Details of calculating polarizability are noted in our prior work.⁵²

Using eq 2 requires the following: (1) determining the $U_{\text{pzc},\lambda}$ for any intermediate λ along the reaction path and (2) a model of both the capacitance and the electric field of the electrode–electrolyte interface. $U_{\text{pzc},\lambda}$ could be calculated directly by determining the work function of the surface/adsorbate system, and using the relationship between work function and surface potential. However, we find it more convenient to recognize that the surface normal dipole moment reliably predicts the shift in work function (i.e., PZC) relative to the bare surface, U_{pzc} as given in the form of eq 4 (and discussed more fully in recent work)⁵²

$$U_{\text{pzc},\lambda} = U_{\text{pzc}} + \frac{\mu_{\lambda}}{\varepsilon_{\text{r}} \varepsilon_{0} A} \tag{4}$$

where $\varepsilon_{\rm r}$ is the relative permittivity of the EDL, ε_0 is the permittivity of vacuum, and A is the area of the model surface slab. The PZC of the bare surface ($U_{\rm pzc}$) without λ in the subscript) is determined from the calculated work function of the bare slab, \varnothing , and converted to the SHE scale, as shown in eq 5

$$U_{\rm pzc}(\rm SHE) = \frac{\varnothing - 4.66}{|e|} \tag{5}$$

where e is the charge of an electron. A value of 4.66 was used to facilitate comparison with the eGC-DFT results. Equations 2, 4, and 5 effectively correct DFT reaction energetics to constant potential (constant work function) using the magnitude of the dipole moment changes along the reaction path.

Determining a model of both the capacitance and the electric field that is representative of the EDL is challenging due to the uncertainty in the interfacial properties during electrocatalytic reaction conditions. A classical parallel plate model (Helmholtz model) is employed to describe the EDL due to its advantage of describing the effects of potential and electrification using two parameters, the dielectric constant, ε_r , and the EDL width (d), as shown in eqs 6 and 7

$$C_{\rm dl} = \frac{\varepsilon_{\rm r} \varepsilon_0 A}{d} \tag{6}$$

$$F_{\lambda} = \frac{U - U_{\text{pzc},\lambda}}{d} \tag{7}$$

Equations 2–7 allow for the calculation of potential-dependent free energies between any two states along the reaction path, for example, by expressing the equation set with λ = transition state and subtracting the same equations expressed for λ = reactant state.

For coupled proton–electron transfer steps (i.e., the C–H and O–H steps), eq 8 shows the form of the potential-dependent activation grand free energy between the transition and reactant state, $\Delta\Omega^{\ddagger}(U')$

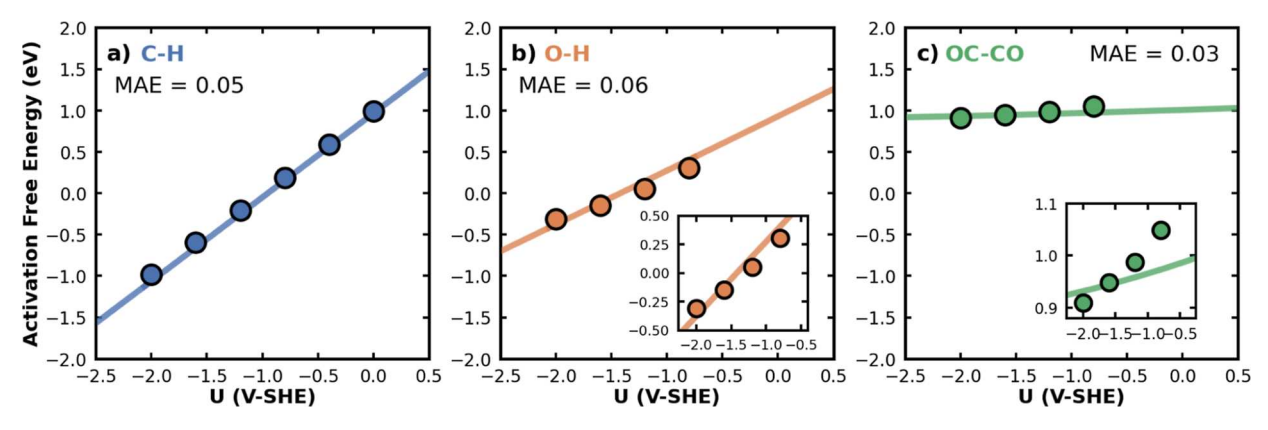


Figure 2. Comparing potential-dependent activation free energies from aGC-DFT (lines) and eGC-DFT (points) for (a) C-H, (b) O-H, and (c) OC-CO bond formations of CO* on Cu(111). aGC-DFT parameters for the EDL are $\varepsilon_r = 78$ and d = 3 Å for C-H and OC-CO and $\varepsilon_r = 78$ and d = 4 Å for O-H. MAE (eV) for each reaction is denoted. Insets for O-H and OC-CO panels highlight differences between the two models at a smaller free energy range.

$$\begin{split} \Delta\Omega^{\ddagger}(U') &= \Delta G^{\ddagger,o} + \text{lel}U' - \frac{1}{2} \frac{\Delta(\mu^2)}{\epsilon A d} + \frac{\Delta\mu}{d} U' \\ &- \frac{\Delta(\mu^2)}{\epsilon A d} + \frac{\Delta\mu}{d} U' + \frac{\Delta(\alpha\mu^2)}{2\epsilon^2 A^2 d^2} - \frac{\Delta(\alpha\mu)}{\epsilon A d^2} U' \\ &+ \frac{1}{2} \frac{\Delta\alpha}{d^2} {U'}^2 \end{split} \tag{8}$$

where $U' = U - U_{\rm pzc}$ on the SHE scale assumed at pH = 0. $\Delta G^{\ddagger, \rm o}$ is the uncorrected activation barrier at $U_{\rm pzc}$ of the bare surface, as shown in eq 9

$$\Delta G^{\ddagger,o} = G_{TS*} - G_{A*} - \frac{1}{2}G_{H_2} + |e|U_{pzc} + \Delta \Delta G_{Sol}$$
 (9)

where G_{TS^*} is the free energy of the transition state, G_{A^*} is the free energy of the reactant state (i.e., CO*), and G_{H_2} is the free energy of gas-phase H_2 corrected to 1 atm using the ideal gas approximation.

For nonproton-transfer steps (i.e., the OC-CO step), eqs 10 and 11 are used to compute the potential-dependent activation grand free energies

$$\Delta\Omega^{\ddagger}(U') = \Delta G^{\ddagger,o} - \frac{1}{2} \frac{\Delta(\mu^2)}{\varepsilon A d} + \frac{\Delta \mu}{d} U' - \frac{\Delta(\mu^2)}{\varepsilon A d} + \frac{\Delta \mu}{d} U' + \frac{\Delta(\alpha \mu^2)}{2\varepsilon^2 A^2 d^2} - \frac{\Delta(\alpha \mu)}{\varepsilon A d^2} U' + \frac{1}{2} \frac{\Delta \alpha}{d^2} {U'}^2$$

$$(10)$$

$$\Delta G^{\ddagger,o} = G_{\text{TS}*} - G_{\text{IS}*} + \Delta \Delta G_{\text{Sol}} \tag{11}$$

where the initial state depicts two coadsorbed CO* on the surface. The main difference here is the removal of both the free energy of gas-phase H_2 and the |e|U terms due to a lack of coupled proton–electron transfer.

Solvation in eqs 9 and 11 is only considered short-range solvation from explicit H_2O included within the DFT model (when applicable). Long-range solvation can be incorporated as a correction term $(\Delta\Delta G_{\rm Sol})$ —the difference in solvation free energies between the transition and initial states—to eqs 8 and 9. We computed $\Delta\Delta G_{\rm Sol}$ by running single-point calculations—with and without the implicit model turned on, and with no applied potential—on geometries of the initial states and transition states optimized at -0.8 V-SHE. To facilitate

comparison with the results from eGC-DFT, the values of $\Delta\Delta G_{Sol}$ from CANDLE are used in the aGC-DFT framework. However, a comparison between solvation energies obtained between CANDLE and VASPSol show minimal differences between the two solvation models, as shown in Table S7.

3. RESULTS AND DISCUSSION

Both aGC-DFT and eGC-DFT were used to calculate potential-dependent activation (grand) free energies for CO* reduction on Cu(111) and Cu(100). First, the activation free energies of C–H, O–H, and OC–CO bond formation on Cu(111) computed via the two methods are compared to discuss the advantages and disadvantages between both approaches (Section 3.1). The sensitivity of the calculated activation barriers on the chosen EDL properties is then quantified (Section 3.2). The impact of the chosen EDL properties on the selectivity and activity of C–H vs O–H formation to C_1 products is then investigated in Section 3.3. Considering this sensitivity between C–H vs O–H formations on EDL properties, we briefly discuss opportunities to tune the reaction pathway to favor C–H or O–H formation.

Comparison between aGC-DFT and eGC-DFT. The potential-dependent activation barriers of the three elementary steps (C-H, O-H, and OC-CO) on Cu(111) are shown in Figure 2. We find good agreement between the two methods for all three elementary steps. For the C-H, O-H, and OC-CO steps, respectively, the mean absolute errors (MAEs) are 0.05, 0.06, and 0.03 eV, and the max absolute errors are 0.08, 0.09, and 0.07 eV. The symmetry factors (β) , that is, the slope of the activation barrier versus potential, are also consistent between the two methods. Linear slopes fitted to eGC-DFT data points yield β of 0.99, 0.51, and 0.11 for the C-H, O-H, and OC-CO steps, respectively. The first-order derivative in the aGC-DFT formalism (eqs 8 and 10) gives β of 1.02, 0.66, and 0.05, respectively. Note that Figure 2 shows negative activation barriers at the most reductive potentials considered due to the analytical extrapolation approach, though the reaction should instead be taken to be barrierless at such potentials were these values used to predict rate constants.

We posit that the small energetic differences between the two methods arise from a few computational technicalities. The first difference comes from changing the core electron description from the GRBV pseudopotential to the PAW method, which pertains to our particular setup of running eGC-DFT in JDFTx and aGC-DFT in VASP. Second, aGC-DFT uses solvation free energy differences between uncharged states, which were assumed to have no potential dependence. The eGC-DFT calculations, however, might have picked up small changes in solvation free energy differences with applied potential due to, for example, changes in the cavity volume (electronic density-based) of different adsorbates. Lastly, the ion distribution is inherently different between the two methods. aGC-DFT uses a planar Helmholtz-like ionic layer with a prescribed distance from the electrode. eGC-DFT, instead, uses an exponentially decaying profile of ions versus electrode distance, as described by the linearized Poisson-Boltzmann framework. Thus, the value of d used between eGC-DFT and aGC-DFT does not need to be identical. The minimization of the MAE of O-H bond formation utilized d =4 Å within the aGC-DFT framework, which is different than the Debye length used in the eGC-DFT calculation (d = 3 Å). Figures S1-S3 denote further discussion of how tuning the EDL width affects the comparison between eGC-DFT and aGC-DFT on Cu(111) and Cu(100) surfaces.

Despite the differences in a few computational technicalities, the observed good agreement in Figure 2 highlights the fidelity of the aGC-DFT approach in predicting potential-dependent activation barriers. This result attests to the approach of compartmentalizing the potential-dependent energetics into underlying physical interactions (eqs 8 and 10). The data in Figure 3 shows the values of the various terms in the aGC-DFT calculated barriers at two different potentials.

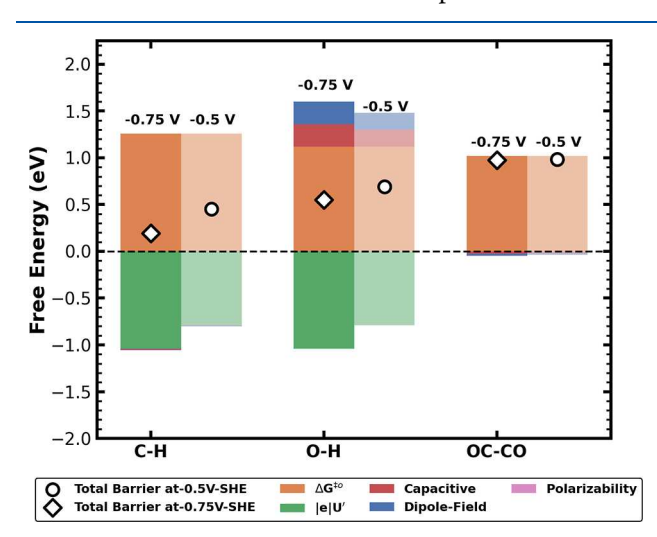


Figure 3. Compartmentalization of potential-dependent activation free energies from aGC-DFT for C–H, O–H, and OC–CO bond formation of CO* on Cu(111). aGC-DFT parameters for the EDL are $\varepsilon_{\rm r}=78$ and d=3 Å for C–H and OC–CO and $\varepsilon_{\rm r}=78$ and d=4 Å for O–H. Potentials are referenced to the SHE. Transparent colored bars refer to free energies at –0.5 V-SHE, whereas the fully shaded bars refer to free energies at –0.75 V-SHE.

The data in Figure 3 shows that the potential dependence of the activation energies of C–H bond formation is largely due to the linear shift in the energy of the electron. The capacitive and field interaction terms are negligible due to the insignificant dipole moment change ($\Delta\mu=0.02$ eÅ) during C–H bond formation. As a result, this reaction step observes a value of $\beta\sim1$ as the total barrier changes from -0.75 V-SHE to -0.5 V-SHE. However, the capacitive and field interaction

terms significantly contribute to the overall barrier for O-H bond formation due to the large dipole moment change ($\Delta \mu$ = -0.68 eÅ). For $\varepsilon_r = 78$ and d = 4 Å, both the correction to constant voltage (capacitive) and dipole-field interactions increase the activation barrier at -0.5 and -0.75 V-SHE. Considering all potential-dependent contributions, O-H bond formation results in a value of β = 0.66. Though the eGC-DFT method shows a similar symmetry coefficient, the aGC-DFT method provides additional insight into how this value arises from a combination of the capacitive and dipole-field corrections with the explicit faradaic term. The OC-CO bond formation, despite being a nonfaradaic step, shows a small potential dependence ($\beta = 0.04$) that is largely due to the capacitive and dipole-field interactions. All reactions observed in this work have negligible changes in polarizability, resulting in the polarizability contribution on the overall barrier to be insignificant (i.e., 0.002 eV for OC-CO at -0.75 V-SHE). This compartmentalization approach greatly benefits the interpretation and rationalization of applied potential and EDL effects on electrocatalytic kinetics and thermodynamics.

The aGC-DFT approach also proves superior in terms of computational cost due to its simplicity. By rough estimation, using eGC-DFT to produce the discrete data points for C-H and O-H in Figure 2a,b costs about 12 and 8 times more, respectively, than applying aGC-DFT. Multiplying these factors by the number of elementary steps for CO₂RR in Figure 1, it becomes a comparison of months versus years for time spent tackling mechanistic studies between the two methods. More pertinent here, the lower cost of using aGC-DFT also allows for tractable sensitivity analysis of EDL parameters on reaction energetics (Section 3.2). Recreating the data in Figure 2 for different dielectric constants or ion distributions with eGC-DFT requires rerunning all the DFT calculations, whereas aGC-DFT predicts changes in barriers with these properties analytically without additional DFT calculations.

Of course, the eGC-DFT approach is not without its inherent benefits, despite having a much higher computational cost. Modeling elementary reaction steps at fixed applied potentials enables direct examination of potential-dependent atomic geometries and electronic structures (i.e., more than just energetics). If a detailed analysis of potential-dependent electronic structures such as charge densities and density of states is desired, eGC-DFT can provide these. Certain absorbate geometries will not be optimizable without explicit applied potential. 28,69 For example, the final state and transition state for the OC-CO step on Cu(111) could not be geometrically optimized unless enough negative charges were applied (i.e., at and below -0.8 V-SHE, as shown in Figure 2). eGC-DFT can locate such states directly because the inclusion of continuum solvation screens for repulsive periodic cell-to-cell interactions that can make highly polar states unstable. A hybrid approach, in which eGC-DFT (or, simply, adding charge and continuum solvation into a DFT calculation) is used to locate such states, followed by an aGC-DFT workup of the properties of such states taken from singlepoint calculations, is also an inviting option.

Similar conclusions for reactions on Cu(100) are shown in Supporting Information, Note 4.

3.2. Sensitivity of Calculated Barriers Based on the EDL Properties. The data in Figure 4 shows the sensitivity of the potential-dependent activation energies of the three reaction steps of CO* reduction on Cu(111) surface using

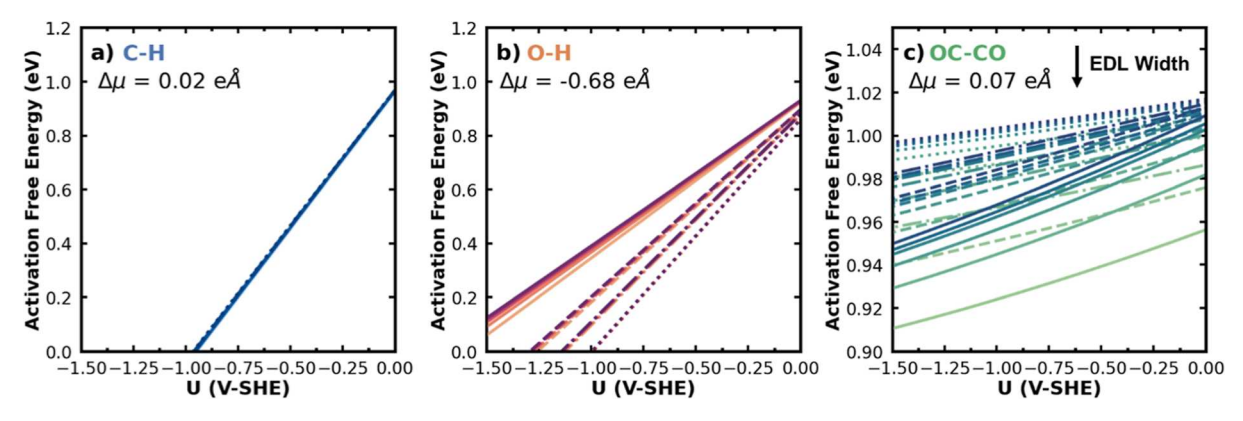


Figure 4. Sensitivity of potential-dependent activation barriers based on approximated values of the EDL properties for (a) C–H, (b) O–H, and (c) OC–CO bond formations of CO* on Cu(111). aGC-DFT framework modeled the EDL using values $\varepsilon_r = 1, 2, 4, 8, 13$, and 78 and d = 3, 4.5, 6, and 10 Å for all plots. Darker colored lines indicate larger dielectric constants. Solid lines correspond to d = 3 Å, dashed lines correspond to d = 4.5 Å, dashed-dotted lines correspond to d = 6 Å, and dotted lines correspond to d = 10 Å, as denoted by the depicted arrows. Dipole moment changes $(\Delta \mu)$ between the initial and transition states for each reaction are also given in each subpanel.

the aGC-DFT approach. The magnitude of the dipole moment change along the reaction path is indicative of the sensitivity of activation barriers to EDL properties. The activation barrier for C-H bond formation (Figure 4a) is not sensitive to the approximated EDL properties because of the insignificant dipole moment change during the reaction. C-H formation shows a slope of barrier with potential (symmetry factor, β) of ~1 from both eGC-DFT and aGC-DFT, as the transition state resembles that of a chemical C-H bond formation step, following a completed electrochemical proton adsorption step. However, the O-H bond formation barrier shows significant sensitivity to the $\varepsilon_{\rm r}$ and EDL width values because of the significant dipole moment change along the reaction path (β varies between 1 and 0.54 across the values of $\varepsilon_{\rm r}$ and d considered in Figure 4, as shown in Supporting Information). The activation energy span shown at -0.95 V-SHE is approximately 0.4 eV for $\varepsilon_r = 78$ (dark purple) from d = 10to 3 Å (dashed dot to solid), resulting in a substantial change in the rate constant by a factor of approximately 5,790,000 at room temperature. For a constant value of d = 3 Å, the activation energy spans by approximately 0.1 eV for $\varepsilon_r = 1$ to 78 at −0.95 V-SHE.

The data in Figure 4c shows that OC–CO bond formation, a nonfaradaic chemical step, exhibits sensitivity based on the chosen EDL properties, though at a much smaller range of \sim 0.1 eV. Decreasing both the EDL width and the dielectric constant leads to a potential dependence of the activation energy to form the OCCO* dimer (β = 0 to 0.04). While the activation energy span is about 0.1 eV, tuning the EDL properties can alter the rate by a factor of approximately 50 at room temperature. Supporting Information, Note 5, shows how the symmetry factor changes as the EDL properties are varied on both Cu(111) and Cu(100) for the reduction of CO*.

Overall, the properties of the solvent and the distribution of ions can impact electrokinetics. The large sensitivity of DFT-predicted activation free energy barriers for elementary steps with large dipole moment changes is alarming because the known values of the solvent properties and ion distributions are needed to determine the operable activation barrier. However, the effective solvent dielectric properties and ion distributions within the EDL will vary with metal, surface facet, and electrolyte composition, and determining such values for

any specific system is a daunting task both experimentally and computationally.

Without knowledge of solvent properties and ion distribution, the uncertainty of DFT-predicted activation free energy barriers of many elementary steps is large. Experimental and computational studies show the effective dielectric constant of water near a metal surface may be closer to 2 than to 78.70-72 Neither Helmholtz nor Poisson-Boltzmann models of counterion distribution agree with observed potential-dependent capacitances, and the applicable counterion distribution for any given electrolyte/electrode combination is unknown. Best practices in DFT calculations should test and report the sensitivity of reported activation barriers (and elementary reaction energies) to these parameters. Simply quantifying the extent to which the surface normal dipole moment varies along the reaction coordinate examined predicts well this sensitivity. The aGC-DFT approach shows that both the constantpotential and dipole-field terms in eqs 2, 8, and 10 are dictated by the dipole moment change.

Supporting Information, Note 6, shows equivalent data on Cu(100), both showing similar qualitative conclusions w.r.t sensitivity based on chosen EDL properties.

3.3. EDL Properties Affect Selectivity and Activity to C₁ Products. The data in Figure 5 shows an example where tuning the properties of the EDL impacts the selectivity and activity of reactions toward C₁ products. C-H and O-H bond formation have the same barrier at approximately -0.3 V-SHE if $\varepsilon_r = 78$ and counterion distance = 6 Å (dashed-lines) is used to model the EDL. Below this potential, C-H formation outcompetes the O-H formation. Atomic force microscope and classical molecular dynamics studies have reported that the dielectric constant may be closer to $\varepsilon_{\rm r}=2.^{70-72}$ If values $\varepsilon_{\rm r}=2$ and d = 3 Å are used to represent the EDL, O-H bond formation becomes competitive above approximately -0.15 V-SHE. Altering the interfacial properties of the EDL can alter the selectivity between products formed from C-H and O-H bond reaction paths. Additionally, the activation energy of O-H bond formation is shown to change by approximately 0.2 eV based on the set of EDL parameters, suggesting that the rate constant can change by up to a factor of 2400 at room temperature. Although predicting quantitative conclusions regarding O-H formation is difficult due to its high sensitivity, the ability to alter the activation energy by tuning the

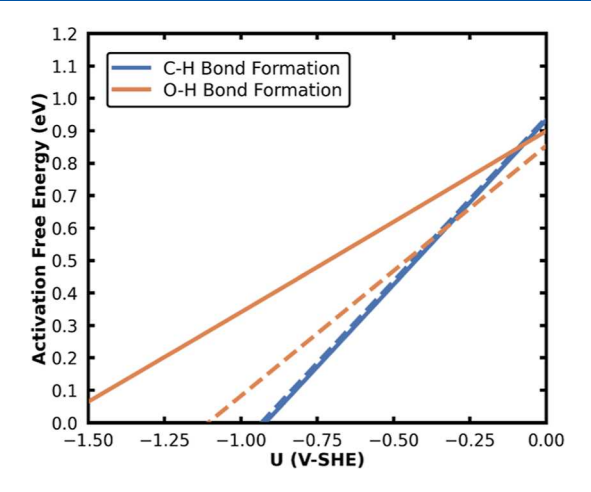


Figure 5. Comparing potential-dependent activation barriers for C–H bond formation (blue) and O–H bond formation (orange) on Cu(111). Solid line corresponds to values of $\varepsilon_{\rm r}=2$ and d=3 Å and dashed lines correspond to $\varepsilon_{\rm r}=78$ and d=6 Å.

electrolyte properties of the EDL is a unique opportunity to improve the activity and selectivity in electrocatalysis.

Figure S8 shows the same data as for Figure 5 but instead for Cu(100), qualitatively showing that tuning the EDL properties has implications on selectivity and activity toward C_1 products.

4. CONCLUSIONS

An aGC-DFT approach was used to quantify the sensitivity of grand activation free energy barriers for electrocatalytic CO₂ reduction reactions on Cu to continuum EDL model parameters. The potential-dependent activation barriers for OC-H, CO-H, and OC-CO bond formation on Cu(111) and Cu(100) were determined using the aGC-DFT approach. We validated this analytical formalism by comparing results against eGC-DFT calculations, highlighting the potentialdependent energetics being captured by compartmentalized interactions between the adsorbates and the EDL. Being much more computationally efficient, the aGC-DFT approach is well-suited for analyzing the sensitivity of DFT-computed electrocatalytic reaction energetics to EDL properties. DFTcomputed electrocatalytic reaction energetics are often highly sensitive to EDL properties, whether an aGC-DFT or eGC-DFT approach is used. The aGC-DFT methods make these dependencies apparent and analytically accessible, rather than requiring repeated eGC-DFT calculations performed with varying EDL properties.

The dipole moment change along the reaction path is indicative of the sensitivity of reaction paths to the approximated values of the EDL properties. Reactions with insignificant dipole moment changes (e.g., C-H bond formation) show minimal sensitivity to the approximated values of the EDL properties. For reactions with larger dipole moment changes (e.g., O-H bond formation), the activation barriers have considerable sensitivity to what values are used to approximate the EDL properties. Until we know the interfacial properties of the electrode-electrolyte interface, we must live with this uncertainty in these parameters and be transparent about this sensitivity when performing atomistic modeling. Rather than tuning EDL parameters to achieve "the right value" or for "a conclusion to match experiment", computational studies in electrocatalysis should standardize practices in

performing sensitivity analysis based on models of the EDL and their parameters.

Although the high sensitivity in predicted activation energies observed in this work can be discouraging, opportunities arise as tuning the EDL environment is predicted to impact electrocatalytic selectivity and activity. Electrolyte engineering strategies for electrocatalysis have been studied, such as altering the identity of the ion and using ionic liquids and mixed solvents. This analytical approach, alongside experimental efforts, can rationally use these opportunities to advance electrocatalytic system design. This work also motivates additional efforts to determine double-layer structures and dielectric properties, for which classical force-field molecular dynamics are well-suited methods. 8,71,76,77

ASSOCIATED CONTENT

Supporting Information

The Supporting Information is available free of charge at https://pubs.acs.org/doi/10.1021/acs.jpcc.4c01457.

Optimized geometries for model reaction paths; eGC-DFT vs aGC-DFT: optimized geometries; eGC-DFT vs aGC-DFT: energetics; compartmentalization of EDL effects; EDL sensitivity on symmetry factor estimation; sensitivity of EDL modeling on Cu(100); and EDL influences on selectivity and activity on Cu(100) (PDF)

AUTHOR INFORMATION

Corresponding Author

Michael J. Janik — Department of Chemical Engineering, The Pennsylvania State University, University Park, Pennsylvania 16802, United States; orcid.org/0000-0001-9975-0650; Email: mjanik@psu.edu

Authors

Andrew Jark-Wah Wong — Department of Chemical Engineering, The Pennsylvania State University, University Park, Pennsylvania 16802, United States

Bolton Tran – Department of Chemical Engineering, University of Michigan, Ann Arbor, Michigan 48109-2136, United States; oorcid.org/0000-0003-2645-4898

Naveen Agrawal — Department of Chemical Engineering, The Pennsylvania State University, University Park, Pennsylvania 16802, United States

Bryan R. Goldsmith – Department of Chemical Engineering, University of Michigan, Ann Arbor, Michigan 48109-2136, United States; o orcid.org/0000-0003-1264-8018

Complete contact information is available at: https://pubs.acs.org/10.1021/acs.jpcc.4c01457

Author Contributions

§A.J.-W.W. and B.T. contributed equally.

Notes

The authors declare no competing financial interest.

ACKNOWLEDGMENTS

M.J.J., A.J.-W.W., and N.A. acknowledge funding from NSF-CBET 1939464. B.R.G. and B.T. acknowledge the W. M. Keck Foundation for financial support. This work used Bridges at the Pittsburgh Supercomputing Center and Expanse at the San Diego Supercomputing Center through allocation CTS150057 from the Advanced Cyberinfrastructure Coordination Ecosys-

tem: Services and Support (ACCESS) program, which is supported by the National Science Foundation grants #2138259, #2138286, #2138307, #2137603, and #2138296. 78

REFERENCES

- (1) Nørskov, J. K.; Rossmeisl, J.; Logadottir, A.; Lindqvist, L.; Kitchin, J. R.; Bligaard, T.; Jónsson, H. Origin of the Overpotential for Oxygen Reduction at a Fuel-Cell Cathode. *J. Phys. Chem. B* **2004**, *108* (46), 17886–17892.
- (2) Wong, A. J.-W.; Miller, J. L.; Perdue, B.; Janik, M. J. Investigating the Electrocatalytic Reduction of 2,4,6-Tri-Nitro-Toluene (TNT) Using Density Functional Theory Methods. *Green Chem.* **2023**, 25, 5097–5112.
- (3) Wong, A. J.-W.; Miller, J. L.; Janik, M. J. Elementary Mechanism for the Electrocatalytic Reduction of Nitrobenzene on Late-Transition-Metal Surfaces from Density Functional Theory. *Chem Catal.* **2022**, 2 (6), 1362–1379.
- (4) Ramos, N. C.; Manyé Ibáñez, M.; Mittal, R.; Janik, M. J.; Holewinski, A. Combining Renewable Electricity and Renewable Carbon: Understanding Reaction Mechanisms of Biomass-Derived Furanic Compounds for Design of Catalytic Nanomaterials. *Acc. Chem. Res.* **2023**, *56* (19), 2631–2641.
- (5) Chen, Z. W.; Chen, L. X.; Wen, Z.; Jiang, Q. Understanding Electro-Catalysis by Using Density Functional Theory. *Phys. Chem. Chem. Phys.* **2019**, 21 (43), 23782–23802.
- (6) Li, H.; Reuter, K. Active-Site Computational Screening: Role of Structural and Compositional Diversity for the Electrochemical CO2 Reduction at Mo Carbide Catalysts. *ACS Catal.* **2020**, *10* (20), 11814–11821.
- (7) Schwarz, K.; Sundararaman, R. The Electrochemical Interface in First-Principles Calculations. *Surf. Sci. Rep.* **2020**, 75 (2), 100492.
- (8) Sundararaman, R.; Vigil-Fowler, D.; Schwarz, K. Improving the Accuracy of Atomistic Simulations of the Electrochemical Interface. *Chem. Rev.* **2022**, *122* (12), 10651–10674.
- (9) Gauthier, J. A.; Ringe, S.; Dickens, C. F.; Garza, A. J.; Bell, A. T.; Head-Gordon, M.; Nørskov, J. K.; Chan, K. Challenges in Modeling Electrochemical Reaction Energetics with Polarizable Continuum Models. *ACS Catal.* **2019**, 9 (2), 920–931.
- (10) Dudzinski, A. M.; Diesen, E.; Heenen, H. H.; Bukas, V. J.; Reuter, K. First Step of the Oxygen Reduction Reaction on Au(111): A Computational Study of O2 Adsorption at the Electrified Metal/Water Interface. ACS Catal. 2023, 13 (18), 12074–12081.
- (11) Bender, J. T.; Petersen, A. S.; Østergaard, F. C.; Wood, M. A.; Heffernan, S. M. J.; Milliron, D. J.; Rossmeisl, J.; Resasco, J. Understanding Cation Effects on the Hydrogen Evolution Reaction. *ACS Energy Lett.* **2023**, *8*, 657–665.
- (12) Chen, L. D. Cations Play an Essential Role in CO2 Reduction. *Nat. Catal.* **2021**, *4* (8), 641–642.
- (13) Briega-Martos, V.; Sarabia, F. J.; Climent, V.; Herrero, E.; Feliu, J. M. Cation Effects on Interfacial Water Structure and Hydrogen Peroxide Reduction on Pt(111). ACS Meas. Sci. Au 2021, 1 (2), 48–55.
- (14) Resasco, J.; Chen, L. D.; Clark, E.; Tsai, C.; Hahn, C.; Jaramillo, T. F.; Chan, K.; Bell, A. T. Promoter Effects of Alkali Metal Cations on the Electrochemical Reduction of Carbon Dioxide. *J. Am. Chem. Soc.* 2017, 139 (32), 11277–11287.
- (15) Ringe, S.; Clark, E. L.; Resasco, J.; Walton, A.; Seger, B.; Bell, A. T.; Chan, K. Understanding Cation Effects in Electrochemical CO2 Reduction. *Energy Environ. Sci.* **2019**, *12* (10), 3001–3014.
- (16) Waegele, M. M.; Gunathunge, C. M.; Li, J.; Li, X. How Cations Affect the Electric Double Layer and the Rates and Selectivity of Electrocatalytic Processes. *J. Chem. Phys.* **2019**, *151* (16), 160902.
- (17) Ovalle, V. J.; Hsu, Y.-S.; Agrawal, N.; Janik, M. J.; Waegele, M. M. Correlating Hydration Free Energy and Specific Adsorption of Alkali Metal Cations during CO2 Electroreduction on Au. *Nat. Catal.* **2022**, *5* (7), 624–632.

- (18) Ringe, S. Cation Effects on Electrocatalytic Reduction Processes at the Example of the Hydrogen Evolution Reaction. *Curr. Opin. Electrochem.* **2023**, 39, 101268.
- (19) McCrum, I. T.; Janik, M. J. pH and Alkali Cation Effects on the Pt Cyclic Voltammogram Explained Using Density Functional Theory. *J. Phys. Chem. C* **2016**, *120*, 457–471.
- (20) Ojha, K.; Doblhoff-Dier, K.; Koper, M. T. M. Double-Layer Structure of the Pt(111)-Aqueous Electrolyte Interface. *Proc. Natl. Acad. Sci. U.S.A.* **2022**, *119* (3), No. e2116016119.
- (21) Pérez-Gallent, E.; Marcandalli, G.; Figueiredo, M. C.; Calle-Vallejo, F.; Koper, M. T. M. Structure- and Potential-Dependent Cation Effects on CO Reduction at Copper Single-Crystal Electrodes. *J. Am. Chem. Soc.* **2017**, *139* (45), 16412–16419.
- (22) Mathanker, A.; Yu, W.; Singh, N.; Goldsmith, B. R. Effects of Ions on Electrocatalytic Hydrogenation and Oxidation of Organics in Aqueous Phase. *Curr. Opin. Electrochem.* **2023**, *40*, 101347.
- (23) Nitopi, S.; Bertheussen, E.; Scott, S. B.; Liu, X.; Engstfeld, A. K.; Horch, S.; Seger, B.; Stephens, I. E. L.; Chan, K.; Hahn, C.; Nørskov, J. K.; Jaramillo, T. F.; Chorkendorff, I. Progress and Perspectives of Electrochemical CO2 Reduction on Copper in Aqueous Electrolyte. *Chem. Rev.* **2019**, *119* (12), 7610–7672.
- (24) Hori, Y.; Wakebe, H.; Tsukamoto, T.; Koga, O. Electrocatalytic Process of CO Selectivity in Electrochemical Reduction of CO2 at Metal Electrodes in Aqueous Media. *Electrochim. Acta* **1994**, 39 (11–12), 1833–1839.
- (25) Hori, Y.; Takahashi, R.; Yoshinami, Y.; Murata, A. Electrochemical Reduction of CO at a Copper Electrode. *J. Phys. Chem. B* **1997**, *101* (36), 7075–7081.
- (26) Peterson, A. A.; Abild-Pedersen, F.; Studt, F.; Rossmeisl, J.; Nørskov, J. K. How Copper Catalyzes the Electroreduction of Carbon Dioxide into Hydrocarbon Fuels. *Energy Environ. Sci.* **2010**, 3 (9), 1311–1315.
- (27) Kuhl, K. P.; Cave, E. R.; Abram, D. N.; Jaramillo, T. F. New Insights into the Electrochemical Reduction of Carbon Dioxide on Metallic Copper Surfaces. *Energy Environ. Sci.* **2012**, *5* (5), 7050–7059
- (28) Montoya, J. H.; Shi, C.; Chan, K.; Nørskov, J. K. Theoretical Insights into a CO Dimerization Mechanism in CO2 Electroreduction. *J. Phys. Chem. Lett.* **2015**, *6* (11), 2032–2037.
- (29) Kortlever, R.; Shen, J.; Schouten, K. J. P.; Calle-Vallejo, F.; Koper, M. T. M. Catalysts and Reaction Pathways for the Electrochemical Reduction of Carbon Dioxide. *J. Phys. Chem. Lett.* **2015**, *6* (20), 4073–4082.
- (30) Cheng, T.; Xiao, H.; Goddard, W. A. I. Free-Energy Barriers and Reaction Mechanisms for the Electrochemical Reduction of CO on the Cu(100) Surface, Including Multiple Layers of Explicit Solvent at pH 0. *J. Phys. Chem. Lett.* **2015**, *6* (23), 4767–4773.
- (31) Lum, Y.; Cheng, T.; Goddard, W. A. I.; Ager, J. W. Electrochemical CO Reduction Builds Solvent Water into Oxygenate Products. J. Am. Chem. Soc. 2018, 140 (30), 9337–9340.
- (32) Feaster, J. T.; Shi, C.; Cave, E. R.; Hatsukade, T.; Abram, D. N.; Kuhl, K. P.; Hahn, C.; Nørskov, J. K.; Jaramillo, T. F. Understanding Selectivity for the Electrochemical Reduction of Carbon Dioxide to Formic Acid and Carbon Monoxide on Metal Electrodes. *ACS Catal.* **2017**, *7* (7), 4822–4827.
- (33) Liu, X.; Schlexer, P.; Xiao, J.; Ji, Y.; Wang, L.; Sandberg, R. B.; Tang, M.; Brown, K. S.; Peng, H.; Ringe, S.; Hahn, C.; Jaramillo, T. F.; Nørskov, J. K.; Chan, K. pH Effects on the Electrochemical Reduction of CO(2) towards C2 Products on Stepped Copper. *Nat. Commun.* **2019**, *10* (1), 32.
- (34) Garza, A. J.; Bell, A. T.; Head-Gordon, M. Mechanism of CO2 Reduction at Copper Surfaces: Pathways to C2 Products. *ACS Catal.* **2018**, 8 (2), 1490–1499.
- (35) Chernyshova, I. V.; Somasundaran, P.; Ponnurangam, S. On the Origin of the Elusive First Intermediate of CO2 Electroreduction. *Proc. Natl. Acad. Sci. U.S.A.* **2018**, *115* (40), E9261–E9270.
- (36) Schouten, K. J. P.; Kwon, Y.; van der Ham, C. J. M.; Qin, Z.; Koper, M. T. M. A new mechanism for the selectivity to C1 and C2

- species in the electrochemical reduction of carbon dioxide on copper electrodes. *Chem. Sci.* **2011**, *2*, 1902–1909.
- (37) Nie, X.; Esopi, M. R.; Janik, M. J.; Asthagiri, A. Selectivity of CO2 Reduction on Copper Electrodes: The Role of the Kinetics of Elementary Steps. *Angew. Chem., Int. Ed.* **2013**, 52 (9), 2459–2462.
- (38) Nie, X.; Luo, W.; Janik, M. J.; Asthagiri, A. Reaction Mechanisms of CO2 Electrochemical Reduction on Cu(111) Determined with Density Functional Theory. *J. Catal.* **2014**, *312*, 108–122.
- (39) Luo, W.; Nie, X.; Janik, M. J.; Asthagiri, A. Facet Dependence of CO2 Reduction Paths on Cu Electrodes. *ACS Catal.* **2016**, *6* (1), 219–229.
- (40) Ringe, S.; Hörmann, N. G.; Oberhofer, H.; Reuter, K. Implicit Solvation Methods for Catalysis at Electrified Interfaces. *Chem. Rev.* **2022**, *122* (12), 10777–10820.
- (41) Zhang, Q.; Asthagiri, A. Solvation Effects on DFT Predictions of ORR Activity on Metal Surfaces. Catal. Today 2019, 323, 35–43.
- (42) Maldonado, A. M.; Hagiwara, S.; Choi, T. H.; Eckert, F.; Schwarz, K.; Sundararaman, R.; Otani, M.; Keith, J. A. Quantifying Uncertainties in Solvation Procedures for Modeling Aqueous Phase Reaction Mechanisms. *J. Phys. Chem. A* **2021**, *125* (1), 154–164.
- (43) Li, P.; Jiao, Y.; Huang, J.; Chen, S. Electric Double Layer Effects in Electrocatalysis: Insights from Ab Initio Simulation and Hierarchical Continuum Modeling. *JACS Au* **2023**, 3 (10), 2640–2659.
- (44) Wellendorff, J.; Lundgaard, K. T.; Møgelhøj, A.; Petzold, V.; Landis, D. D.; Nørskov, J. K.; Bligaard, T.; Jacobsen, K. W. Density Functionals for Surface Science: Exchange-Correlation Model Development with Bayesian Error Estimation. *Phys. Rev. B: Condens. Matter Mater. Phys.* **2012**, 85 (23), 235149.
- (45) Wellendorff, J.; Silbaugh, T. L.; Garcia-Pintos, D.; Nørskov, J. K.; Bligaard, T.; Studt, F.; Campbell, C. T. A Benchmark Database for Adsorption Bond Energies to Transition Metal Surfaces and Comparison to Selected DFT Functionals. *Surf. Sci.* **2015**, *640*, 36–44.
- (46) Urrego-Ortiz, R.; Builes, S.; Illas, F.; Calle-Vallejo, F. Gas-Phase Errors in Computational Electrocatalysis: A Review. *EES Catal.* **2024**, 2 (1), 157–179.
- (47) Gautier, S.; Steinmann, S. N.; Michel, C.; Fleurat-Lessard, P.; Sautet, P. Molecular Adsorption at Pt(111). How Accurate Are DFT Functionals? *Phys. Chem. Chem. Phys.* **2015**, *17* (43), 28921–28930.
- (48) Islam, S. M. R.; Khezeli, F.; Ringe, S.; Plaisance, C. An Implicit Electrolyte Model for Plane Wave Density Functional Theory Exhibiting Nonlinear Response and a Nonlocal Cavity Definition. *J. Chem. Phys.* **2023**, *159* (23), 234117.
- (49) Melander, M. M.; Kuisma, M. J.; Christensen, T. E. K.; Honkala, K. Grand-Canonical Approach to Density Functional Theory of Electrocatalytic Systems: Thermodynamics of Solid-Liquid Interfaces at Constant Ion and Electrode Potentials. *J. Chem. Phys.* **2019**, *150* (4), 041706.
- (50) Sundararaman, R.; Letchworth-Weaver, K.; Schwarz, K. A.; Gunceler, D.; Ozhabes, Y.; Arias, T. A. JDFTx: Software for Joint Density-Functional Theory. *SoftwareX* **2017**. *6*. 278–284.
- (51) Melander, M. M.; Wu, T.; Weckman, T.; Honkala, K. Constant Inner Potential DFT for Modelling Electrochemical Systems under Constant Potential and Bias. *npj Comput. Mater.* **2024**, *10* (1), 5.
- (52) Agrawal, N.; Wong, A. J.-W.; Maheshwari, S.; Janik, M. J. An Efficient Approach to Compartmentalize Double Layer Effects on Kinetics of Interfacial Proton-Electron Transfer Reactions. *J. Catal.* **2024**, 430, 115360.
- (53) Hammer, B.; Hansen, L. B.; Nørskov, J. K. Improved Adsorption Energetics within Density-Functional Theory Using Revised Perdew-Burke-Ernzerhof Functionals. *Phys. Rev. B: Condens. Matter Mater. Phys.* **1999**, *59* (11), 7413–7421.
- (54) Garrity, K. F.; Bennett, J. W.; Rabe, K. M.; Vanderbilt, D. Pseudopotentials for High-Throughput DFT Calculations. *Comput. Mater. Sci.* **2014**, *81*, 446–452.

- (55) Monkhorst, H. J.; Pack, J. D. Special Points for Brillouin-Zone Integrations. *Phys. Rev. B: Condens. Matter Mater. Phys.* **1976**, 13 (12), 5188–5192.
- (56) Pack, J. D.; Monkhorst, H. J. Special Points for Brillouin-Zone Integrations—a Reply. *Phys. Rev. B: Condens. Matter Mater. Phys.* 1977, 16 (4), 1748–1749.
- (57) Methfessel, M.; Paxton, A. T. High-Precision Sampling for Brillouin-Zone Integration in Metals. *Phys. Rev. B: Condens. Matter Mater. Phys.* **1989**, 40 (6), 3616–3621.
- (58) Sundararaman, R.; Goddard, W. A., III The Charge-Asymmetric Nonlocally Determined Local-Electric (CANDLE) Solvation Model. *J. Chem. Phys.* **2015**, *142* (6), 064107.
- (59) Henkelman, G.; Uberuaga, B. P.; Jónsson, H. A Climbing Image Nudged Elastic Band Method for Finding Saddle Points and Minimum Energy Paths. *J. Chem. Phys.* **2000**, *113* (22), 9901–9904.
- (60) Hjorth Larsen, A.; Jørgen Mortensen, J.; Blomqvist, J.; Castelli, I. E.; Christensen, R.; Dulak, M.; Friis, J.; Groves, M. N.; Hammer, B.; Hargus, C.; Hermes, E. D.; Jennings, P. C.; Bjerre Jensen, P.; Kermode, J.; Kitchin, J. R.; Leonhard Kolsbjerg, E.; Kubal, J.; Kaasbjerg, K.; Lysgaard, S.; Bergmann Maronsson, J.; Maxson, T.; Olsen, T.; Pastewka, L.; Peterson, A.; Rostgaard, C.; Schiøtz, J.; Schütt, O.; Strange, M.; Thygesen, K. S.; Vegge, T.; Vilhelmsen, L.; Walter, M.; Zeng, Z.; Jacobsen, K. W. The Atomic Simulation Environment—a Python Library for Working with Atoms. J. Phys.: Condens. Matter 2017, 29 (27), 273002.
- (61) Kresse, G.; Hafner, J. Ab Initio Molecular Dynamics for Liquid Metals. *Phys. Rev. B: Condens. Matter Mater. Phys.* **1993**, 47 (1), 558–561.
- (62) Kresse, G.; Hafner, J. Ab Initio Molecular-Dynamics Simulation of the Liquid-Metal-Amorphous-Semiconductor Transition in Germanium. *Phys. Rev. B: Condens. Matter Mater. Phys.* **1994**, 49 (20), 14251–14269.
- (63) Kresse, G.; Furthmüller, J. Efficiency of Ab-Initio Total Energy Calculations for Metals and Semiconductors Using a Plane-Wave Basis Set. *Comput. Mater. Sci.* **1996**, *6* (1), 15–50.
- (64) Kresse, G.; Furthmüller, J. Efficient Iterative Schemes for Ab Initio Total-Energy Calculations Using a Plane-Wave Basis Set. *Phys. Rev. B: Condens. Matter Mater. Phys.* **1996**, 54 (16), 11169–11186.
- (65) Kresse, G.; Joubert, D. From Ultrasoft Pseudopotentials to the Projector Augmented-Wave Method. *Phys. Rev. B: Condens. Matter Mater. Phys.* 1999, 59 (3), 1758–1775.
- (66) Blöchl, P. E. Projector Augmented-Wave Method. *Phys. Rev. B: Condens. Matter Mater. Phys.* **1994**, *50* (24), 17953–17979.
- (67) Mathew, K.; Sundararaman, R.; Letchworth-Weaver, K.; Arias, T. A.; Hennig, R. G. Implicit Solvation Model for Density-Functional Study of Nanocrystal Surfaces and Reaction Pathways. *J. Chem. Phys.* **2014**, *140* (8), 084106.
- (68) Mathew, K.; Kolluru, V. S. C.; Mula, S.; Steinmann, S. N.; Hennig, R. G. Implicit Self-Consistent Electrolyte Model in Plane-Wave Density-Functional Theory. *J. Chem. Phys.* **2019**, *151* (23), 234101.
- (69) Kristoffersen, H. H.; Chan, K. Towards Constant Potential Modeling of CO-CO Coupling at Liquid Water-Cu(1 0 0) Interfaces. *J. Catal.* **2021**, 396, 251–260.
- (70) Fumagalli, L.; Esfandiar, A.; Fabregas, R.; Hu, S.; Ares, P.; Janardanan, A.; Yang, Q.; Radha, B.; Taniguchi, T.; Watanabe, K.; Gomila, G.; Novoselov, K. S.; Geim, A. K. Anomalously Low Dielectric Constant of Confined Water. *Science* **2018**, *360* (6395), 1339–1342.
- (71) Tran, B.; Zhou, Y.; Janik, M. J.; Milner, S. T. Negative Dielectric Constant of Water at a Metal Interface. *Phys. Rev. Lett.* **2023**, *131* (24), 248001.
- (72) Sugahara, A.; Ando, Y.; Kajiyama, S.; Yazawa, K.; Gotoh, K.; Otani, M.; Okubo, M.; Yamada, A. Negative Dielectric Constant of Water Confined in Nanosheets. *Nat. Commun.* **2019**, *10*, 850.
- (73) Gebbie, M. A.; Liu, B.; Guo, W.; Anderson, S. R.; Johnstone, S. G. Linking Electric Double Layer Formation to Electrocatalytic Activity. *ACS Catal.* **2023**, *13*, 16222–16239.

- (74) McEnaney, J. M.; Blair, S. J.; Nielander, A. C.; Schwalbe, J. A.; Koshy, D. M.; Cargnello, M.; Jaramillo, T. F. Electrolyte Engineering for Efficient Electrochemical Nitrate Reduction to Ammonia on a Titanium Electrode. ACS Sustainable Chem. Eng. 2020, 8 (7), 2672–2681.
- (75) Mohandas, N.; Narayanan, T. N.; Cuesta, A. Tailoring the Interfacial Water Structure by Electrolyte Engineering for Selective Electrocatalytic Reduction of Carbon Dioxide. *ACS Catal.* **2023**, *13* (13), 8384–8393.
- (76) Shandilya, A.; Schwarz, K.; Sundararaman, R. Interfacial Water Asymmetry at Ideal Electrochemical Interfaces. *J. Chem. Phys.* **2022**, 156 (1), 014705.
- (77) Zeng, L.; Peng, J.; Zhang, J.; Tan, X.; Ji, X.; Li, S.; Feng, G. Molecular Dynamics Simulations of Electrochemical Interfaces. *J. Chem. Phys.* **2023**, *159* (9), 091001.
- (78) Boerner, T. J.; Deems, S.; Furlani, T. R.; Knuth, S. L.; Towns, J. ACCESS: Advancing Innovation: NSF's Advanced Cyberinfrastructure Coordination Ecosystem: Services & Support. In *Practice and Experience in Advanced Research Computing*; PEARC '23; Association for Computing Machinery: New York, NY, USA, 2023; pp 173–176..